Supporting Information for

Single rare-earth ions as atomic-scale probes in ultra-scaled transistors

Qi Zhang[1,2,5,6]†, Guangchong Hu[2]†, Gabriele G. de Boo[2], Miloš Rančić[3,7], Brett C. Johnson[4], Jeffrey C. McCallum[4], Jiangfeng Du[1,5,6], Matthew J. Sellars[3], Chunming Yin[1,2,5,6*] & Sven Rogge[2]

[1] Hefei National Laboratory for Physical Sciences at the Microscale and Department of Modern Physics, University of Science and Technology of China, Hefei 230026, China

[2] Centre of Excellence for Quantum Computation and Communication Technology, School of Physics, University of New South Wales, Sydney, New South Wales 2052, Australia.

[3] Centre of Excellence for Quantum Computation and Communication Technology, Research School of Physics, Australian National University, Canberra, Australian Capital Territory 0200, Australia.

[4] Centre of Excellence for Quantum Computation and Communication Technology, School of Physics, University of Melbourne, Melbourne, Victoria 3010, Australia

[5] CAS Key Laboratory of Microscale Magnetic Resonance, University of Science and Technology of China, Hefei 230026, China

[6] Synergetic Innovation Center of Quantum Information and Quantum Physics, University of Science and Technology of China, Hefei 230026, China

[7] Quantronics Group, SPEC, CEA Saclay, 91191 Gif-sur-Yvette Cedex, France

†These authors contributed equally to this work.

*E-mail: c.yin@unsw.edu.au

Characterising the strain field of a single Er ion

Fig. S1 shows the simulated spectral response of an Er ion with cubic site symmetry under different stresses. The $^4I_{15/2} \rightarrow {}^4I_{13/2}$ optical transition for Er ions in Si is completely described by the Lea-Leask-Wolf (LLW) crystal field Hamiltonian H_{CF}[1]. The Hamiltonian parameters for well annealed and unstrained tetrahedral symmetry T_d Er sites in Si were determined by Przybylinska et al.[2] From first principles, it is possible to determine the perturbation to this Hamiltonian from a strain field, $\boldsymbol{\sigma} = \sum_{i,j=x,y,z} \sigma_{i,j}$, and electric field, $\boldsymbol{E} = \sum_{i=x,y,z} E_i$. By considering the character table for the T_d point group, one arrives at the following Hamiltonian:

$$\begin{aligned} H = H_{CF} &+ A(\sigma_{xx} + \sigma_{yy} + \sigma_{zz})J^2 \\ &+ B\left[(2\sigma_{zz} - \sigma_{xx} - \sigma_{yy})(2J_z^2 - J^2) + (\sigma_{xx} - \sigma_{yy})(J_x^2 - J_y^2)\right] \\ &+ C\left[\sigma_{xy}\{J_x, J_y\} + \sigma_{xz}\{J_x, J_z\} + \sigma_{yz}\{J_y, J_z\}\right] \\ &+ D[(E_x + E_y)\{J_x, J_y\} + (E_x + E_z)\{J_x, J_z\} + (E_y + E_z)\{J_y, J_z\}] \end{aligned}$$

The xyz coordinate is chosen to be consistent with Si crystalline <100> coordinate. The empirical constants in the perturbation Hamiltonian can be determined with a calibration experiment on an unstrained and well annealed Er-doped Si wafer. The constants *A*, *B* and *C* can be determined by applying a known stress.

Specifically, hydrostatic stress only introduces an isotropic strain tensor with equal diagonal terms ($\sigma_{xx} = \sigma_{yy} = \sigma_{zz}$) and zero non-diagonal terms ($\sigma_{xy} = \sigma_{xz} = \sigma_{yz} = 0$)[3]. So a constant *A* could be directly determined by a hydrostatic stress experiment shown in Fig. S1a. Uniaxial stress along the <100> direction also generates a diagonal strain tensor with non-diagonal

terms equal to zero ($\sigma_{xy} = \sigma_{xz} = \sigma_{yz} = 0$), while a diagonal shear component will result in non-equal diagonal terms. Once *A is known*, *B* could be derived from a uniaxial stress experiment along <100> (Fig. S1b). Uniaxial stress along <111> will introduce a strain tensor with isotropic diagonal terms ($\sigma_{xx} = \sigma_{yy} = \sigma_{zz}$) and non-zero non-diagonal terms, from which the constant *C* could be determined.

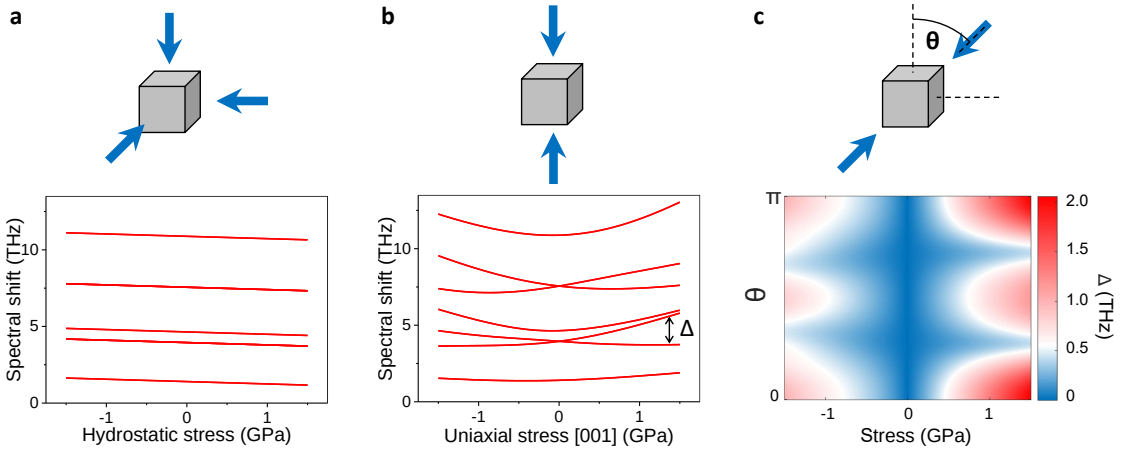

Fig. S1 Spectral shift simulation of cubic Er site under different stresses. a, The hydrostatic stress keeps the crystal symmetry and simply shifts all the transitions linearly. **b,** Uniaxial stress [001] breaks the crystal symmetry, introducing a non-linear dependence and splitting to the crystal levels of the Er site. **c,** The dependence of the level splitting (Δ indicated in b) on uniaxial stress magnitude and polar angle (θ) in the (010) plane.

For the simulation in Fig. S1, the crystal field Hamiltonian parameters are from results reported in Ref. 28 and 29. There is no experimental work directly measuring constants *A*, *B* and *C*, so we set them phenomenologically according to the results from Fig. 4 and spectroscopic measurements of ensemble Er^{3+} ions doped in strained silicon structure[4–6], with $2A = B = 2C = 2$ THz per unit of strain.

Similarly, the constant *D* could be determined with a known electric field. For the above Hamiltonian, it is important to note that both shear stress and electric field have the same phenomenological effect on the Er ion. To distinguish between the electric field and shear stress, tests with different transistor electrodes settings and corresponding finite element simulations might be necessary.

With a *priori* knowledge of the stress Hamiltonian, the determination of the stress tensor in a microscopic voxel has already been demonstrated, using several NV centres in diamond[7]. For cubic Er sites in silicon, however, the lack of non-equivalent site orientations limits the usefulness of comparing neighbouring sites. Instead, each Er ion provides much richer spectroscopic information, given the fourteen (optically accessible) crystal field levels in the $^4I_{13/2}$ manifold. With a resolution of ~ 10 MHz on the optical transitions, it should be possible to determine very precisely the magnitude (but not direction) of the hydrostatic, diagonal and non-diagonal shear strain components by studying all 14 optically accessible levels.

In conjunction with a magnetic field rotation study for each site, some prior knowledge of the overall strain field direction should help determine some of the directional components of the local strain field. Under ideal conditions, it may even be possible to unambiguously determine all 6 independent components of the local strain tensor $\boldsymbol{\sigma}$ at the location of some sites.

The strain calibration test

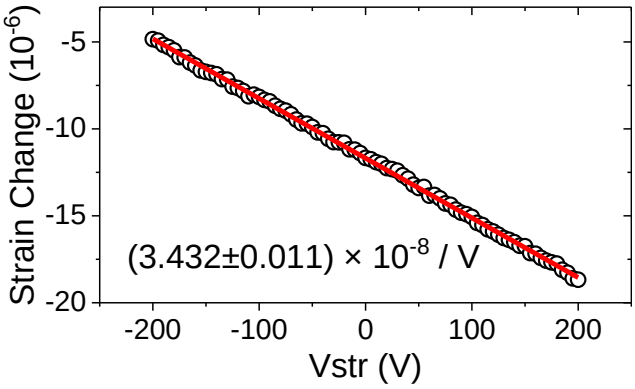

Fig. S2 Measurements with the strain gauge reveal a linear dependence of the actuator-induced strain on *V*str. The circles are averaged data from 5 scans back and forth between *V*str=+/- 200 V.

29-Si hyperfine interaction on the spectra

We have not observed any splitting due to hyperfine interaction between Er and a nearby 29-Si. Based on magnetic dipole-dipole interaction, the field caused by a 29-Si nucleus at 144 pm is 9e-5 T (interstitial) and at 235 pm it is 2e-5 T (substitutional). For an optical line with a very large delta-g factor of 10, the Zeeman shift slope is about 140 GHz/T, and this would cause a splitting of 12.6 MHz (144 pm) or 2.8 MHz (235 pm). This is smaller than our spectral linewidth (30 MHz). Even if a particular configuration leads to interaction of hundreds of MHz as the reviewer mentioned, given the 29-Si nucleus is a spin ½ system, we would be able to characterize it and remove it from our spectrum.

A set of spectra recorded in a strain tuning measurement

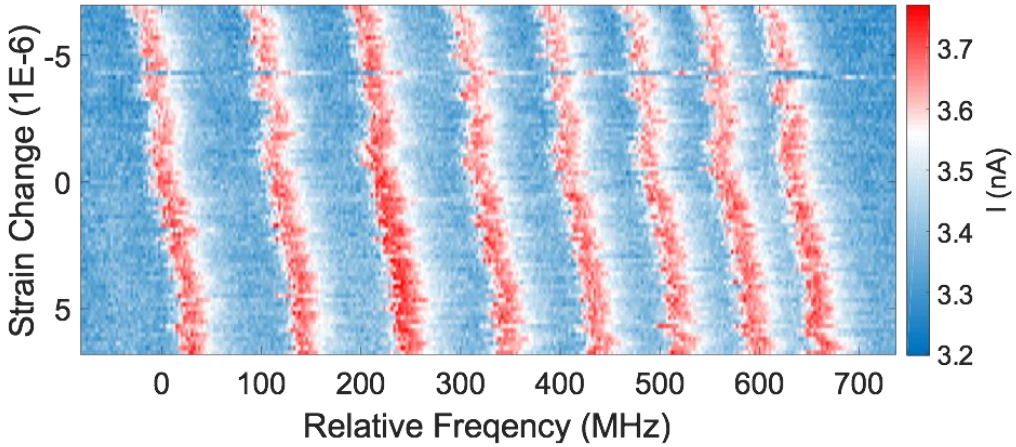

Fig. S3 Spectra recorded for Er-3 as a function of laser frequency and the change in strain (converted from the *V*str value). The colour scale indicates the photo-ionisation current. The abrupt spectral shift at a strain change of -4.3 x 10^{-6} (*V*str = 125 V), is due to a temporary unlock of the cavity-stabilised laser.

Nano-scale strain mapping in a semiconductor device.

Strain engineering could introduce band bending to lower the effective mass of carriers, and enhance their mobility. Thorough knowledge of the strain distribution will provide valuable information on the manufacturing process and provide valuable input parameters for device modelling. There are different ways of measuring strain at different scales[8] but

measurements on the transistor level are definitely the keystone. Below is a comparison between different techniques used for strain characterization.

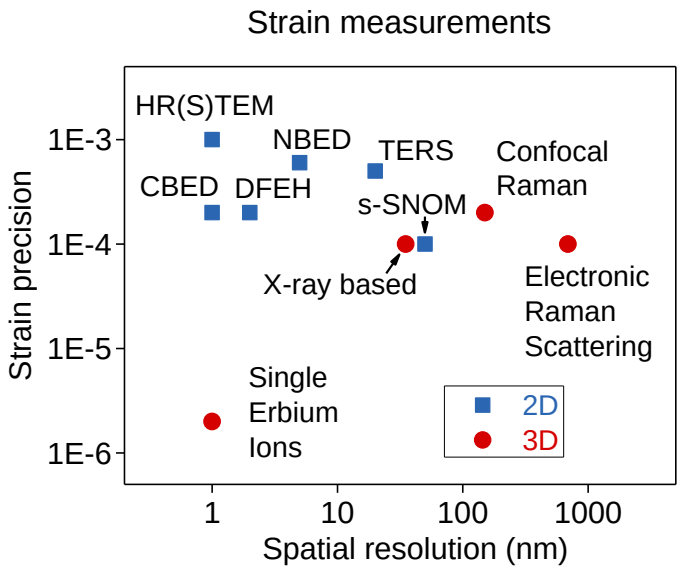

Fig. S4 A comparison of the spatial resolution and strain precision between our method and other reported strain detecting techniques. The blue squares indicate techniques capable of only 2D mapping, while the red dots represent 3D mapping techniques. List of abbreviations: CBED, convergent-beam electron diffraction; NBED, nano-beam electron diffraction; HR(S)TEM, high-resolution (scanning) TEM; DFEH, dark-field electron holography; TERS, tip enhanced Raman scattering microscopy; s-SNOM, scattering-type scanning near-field optical microscopy.

Non-destructive strain information can be obtained with X-ray diffraction[8–11]. However, its spatial resolution is typically tens of nanometres even if huge synchrotron facilities are employed[12]. Recent results show that X-ray ptychography reaches a high lateral resolution of 14.6 nm, which could be applied to strain mapping[14]. However, complex simulations and reference samples are needed.

There are several strain sensing methods[15,16] based on transmission electron microscopy (TEM). Overall, they have the best spatial resolution and accuracy. But dedicated sample preparation is necessary for this technique. Specimens need to be milled to electron transparency thicknesses of 100-300 nm. This procedure is time-consuming and likely to cause strain relaxation. Again, complex simulations and reference samples are required.

Confocal Raman based techniques are more suitable to strain analysis on a larger scale. Generally, its spatial resolution is not enough for transistor level mapping. Cryogenic temperatures are needed to achieve 10^{-4} order accuracy[17]. Spatial resolution could be improved with scattering-type scanning near-field optical microscopy[18] (s-SNOM) or tip enhance Raman spectroscopy[19] (TERS). But, they are limited to shallow subsurface detection because of the near-field penetration depth (~20 nm).

Compared to the above approaches, the outstanding advantages of the method described here are the combination of high precision, low perturbation and promising potential of high resolution 3D mapping. This method introduces only a small perturbation to the specimen, including illumination with a 1550 nm laser well below silicon band gap energy, and Er^{3+} ion implantation with doping concentration much lower than that normally employed by the semiconductor industry. No destructive sample treatments like milling are required. As silicon is transparent to 1550 nm light, this method could access regions much deeper below the

surface, which is critical to measurements for further 3D integrated circuits with multiple stacks.

The ionic radii of Er^{3+} ion is 103 pm, not too large for Si-Si bond length of 235 pm. While the 4f-orbitals of Er^{3+} ions don't bond with sp^3 orbitals of silicon, leading to their random positioning and various sites. This randomness could be depressed by proper annealing. Besides, the existence of an Er ion in silicon lattice may affect the local strain, however, this perturbation is an intrinsic part of the site structure and will be separated from the strain detection as a background in the Hamiltonian simulation. Various Er sites would be evaluated from analysis of crystal levels structure, hyperfine structure and Zeeman/Stark/strain coefficients. These tests would be use in the Hamiltonian simulation for each Er site and to determine the site configuration. Building up such a database will need quite a lot of tests on specially-designed devices with well controllable electric/strain fields. Once the database is well established, Er^{3+} sites with small inhomogeneous broadening could be utilised for the electric field and strain detection.

As the probes are better to reside with average distance of ~20nm, only a few probes will be present in a single transistor. Test on many transistors are required to get the full map. Here we argue that the minimum transistor number N is not dependent on the channel volume V, given the atomic probe density n and the imaging grid size l. The probability of finding no ions in a specific grid after searching in N_t transistors is $(1-1/N_g)^{N_t \cdot N_i}$, where $N_g = V/l^3$ is the number of grids per channel and $N_i = V \cdot n$ is the average number of ions per channel. As $(1-1/N_g)^{2.3\,N_g} \sim 10\%$ when N_g is a large number, to occupy 90% of the grids, we have $N_t \cdot N_i = 2.3\,N_g$ thus $N_t = 2.3/n \cdot l^3$. For n = 1.7×10^{17} cm^{-3}, and l = 2 nm as exampled in the main text, N_t = 1700.

Imaging resolution

Imaging resolution of this method relies on the resolution of locating the Er^{3+} ions in the channel. Two methods could be used to provide the 3D magnetic field gradient. Here we respectively prospect their uses in locating our atomic probes.

Scanning magnetic tip is well applied in magnetic resonance force microscopy[20] and NV-MRI[21] for single spins imaging with nanometer resolution. By comparing the Zeeman responses of two different spins as the tip scanned, their relative position can be determined three-dimensionally with resolution better than 1 nm. One important feature of this method, as noted in ref. [21], is that it has no reliance on magnetic field modelling. Here we could employ the same principle to derive the relative positons between those Er^{3+} ions in the same transistor. The optical linewidth of Er^{3+} ions observed here (30 MHz) is larger than the spin-transition linewidth (~7 MHz) in ref. 21, while thanks to the commonly larger Zeeman coefficients (~10 MHz/Gs), we could still expect the sub-nanometer resolution in distinguishing Er^{3+} ions. However, to know their locations in the channel, tip scanning maps of the transistor geometry are needed for references. This will bring excess uncertainties from AFM mapping and manufacturing variations between different transistors. Another drawback is the difficulty of achieving high-throughput test for large numbers of devices.

An alternative is to fabricate micro-magnetos beside the transistors[22]. It allows high-throughput measurements with multiple transistors testing in parallel. This could be achieved by depositing a strip of cobalt of a width that is similar to the length of the channel next to the pre-fabricated transistor by electron beam lithography and lift-off. Through changing the polarization directions of the magnetos with different external fields, combined with magnetic field modelling, one could get 3D map of the ions. Considering the large magnetic gradients

and Zeeman coefficients, the main limit to achieving high spatial resolution would be the uncertainty of the modelling and the manufacturing variations. However, these uncertainties could be well calibrated with input from high resolution scanning electron microscope, which could provide the geometry parameters of transistors and magnetos with precision down to sub-nanometer[23].

Implantation disturbance to silicon

For the device used in the experiment we performed Er:O co-implantation with respective energies of 400 and 55 keV and ion fluences of 4×10^{12} and 3×10^{13} cm^{-2}. The devices were annealed at 700 °C after implantation. To get doping concentration of ~10^{17} cm^{-3} as discussed in main text, 1×10^{12} cm^{-2} is enough with 400 keV Er ion beam. An empirical relation can be used to roughly estimate the global strain induced by ion implantation with hundreds of keV ion energy and moderate fluence before annealing[24]

$$\varepsilon^{\perp}(d) = K\phi F_D(d),$$

where $\varepsilon^{\perp}(d)$ is the perpendicular strain at depth d. K is a parameter reflecting how deposited energy from the incident ion transferred to strain, 3.1 × 10^{-5} Å^3/eV for silicon. ϕ = 1×10^{12} cm^{-2} is the ion dose and $F_D(d)$ is energy deposited per incident ion by nuclear collisions. $F_D(d)$ includes not only the energy deposited directly from the incident ion, but also from secondary process through collision cascade. $F_D(d)$ reaches the maximum at depth normally above where incident ions concentration reaches the maximum. Here we give a rough estimation to the F_{Dmax} by deriving nuclear stopping power S_n (unit eV/Å) from a semi-empirical formula[25]:

$$S_n = \frac{0.5\ \ln(1+\varepsilon)}{\varepsilon+0.10718\varepsilon^{0.37544}}\ \frac{8.462Z_1Z_2M_1}{(M_1+M_2)(Z_1^{2/3}+Z_1^{2/3})^{1/2}}\frac{6.022\,\rho}{M_2},$$

where the reduce energy of an ion, ε, is defined as

$$\varepsilon = \frac{32.53M_2E}{Z_1Z_2(M_1+M_2)(Z_1^{2/3}+Z_1^{2/3})^{1/2}}.$$

E is the ion energy in keV, Z_1 and Z_2 are the ion and target atomic numbers, M_1 and M_2 are the ion and target masses in amu, and ρ = 2.33 g/cm^{-3} is the silicon mass density. For 400 keV ^{168}Er ions injected to silicon, S_n = 257.6 eV/Å. We use this as an approximation for F_{Dmax}, and get $\varepsilon^{\perp}_{max}$ = 8×10^{-5}. Strain induced by 55 keV O ions with dose of 8×10^{12} cm^{-2} is 2.9×10^{-5} according to the above calculation. As a note, we intentionally prepared a variety of Er devices with and without oxygen co-implantation and have not observed any impact of oxygen on the linewidth and stability of Er spectra till now. In this demonstration work, devices co-implanted with oxygen were used, but this is not necessary.

References

(1) Lea, K. R.; Leask, M. J. M.; Wolf, W. P. The Raising of Angular Momentum Degeneracy of F-Electron Terms by Cubic Crystal Fields. *J. Phys. Chem. Solids* **1962**, *23* (10), 1381–1405. https://doi.org/10.1016/0022-3697(62)90192-0.

(2) Przybylinska, H.; Jantsch, W.; Suprun-Belevitch, Y.; Stepikhova, M.; Palmetshofer, L.; Hendorfer, G.; Kozanecki, A.; Wilson, R.; Sealy, B. Optically Active Erbium Centers in Silicon. *Phys. Rev. B* **1996**, *54* (4), 2532–2547. https://doi.org/10.1103/PhysRevB.54.2532.

(3) Yu, P. Y.; Cardona, M. *Fundamentals of Semiconductors: Physics and Materials Properties*, Fourth.; Graduate Texts in Physics; Springer Berlin Heidelberg: Berlin, Heidelberg, 2010. https://doi.org/10.1007/978-3-642-00710-1.

(4) Naveed, A. T.; Wright, A. C.; Houghton, D. C.; Peaker, A. R. Erbium-Doped Si 1 − x Ge x / Si Structures for Light Emitting Diodes. **2000**, *15*, 91–97.

(5) Huda, M. Q. Luminescence from Erbium Implanted Silicon–germanium Quantum Wells. *J. Vac. Sci. Technol. B Microelectron. Nanom. Struct.* **1998**, *16* (6), 2928. https://doi.org/10.1116/1.590320.
(6) Ishiyama, T.; Nawae, S.; Komai, T.; Yamashita, Y.; Kamiura, Y.; Hasegawa, T.; Inoue, K.; Okuno, K. Photoluminescence of Er in Strained Si on SiGe Layer. *J. Appl. Phys.* **2002**, *92* (7), 3615–3619. https://doi.org/10.1063/1.1506391.
(7) Grazioso, F.; Patton, B. R.; Delaney, P.; Markham, M. L.; Twitchen, D. J.; Smith, J. M. Measurement of the Full Stress Tensor in a Crystal Using Photoluminescence from Point Defects: The Example of Nitrogen Vacancy Centers in Diamond. *Appl. Phys. Lett.* **2013**, *103* (10). https://doi.org/10.1063/1.4819834.
(8) *International Technology Roadmap for Semiconductors 2.0 Metrology*; 2015.
(9) Pfeifer, M. A.; Williams, G. J.; Vartanyants, I. A.; Harder, R.; Robinson, I. K. Three-Dimensional Mapping of a Deformation Field inside a Nanocrystal. *Nature* **2006**, *442* (7098), 63–66. https://doi.org/10.1038/nature04867.
(10) Robinson, I.; Harder, R. Coherent X-Ray Diffraction Imaging of Strain at the Nanoscale. *Nat. Mater.* **2009**, *8* (4), 291–298. https://doi.org/10.1038/nmat2400.
(11) Newton, M. C.; Leake, S. J.; Harder, R.; Robinson, I. K. Three-Dimensional Imaging of Strain in a Single ZnO Nanorod. *Nat. Mater.* **2010**, *9* (2), 120–124. https://doi.org/10.1038/nmat2607.
(12) Holt, M. V.; Hruszkewycz, S. O.; Murray, C. E.; Holt, J. R.; Paskiewicz, D. M.; Fuoss, P. H. Strain Imaging of Nanoscale Semiconductor Heterostructures with X-Ray Bragg Projection Ptychography. *Phys. Rev. Lett.* **2014**, *112* (16), 1–6. https://doi.org/10.1103/PhysRevLett.112.165502.
(13) Maqbool, M. S.; Hoxley, D.; Phillips, N. W.; Coughlan, H. D.; Darmanin, C.; Johnson, B. C.; Clark, J. N.; Abbey, B. Nanoscale Mapping of the Three-Dimensional Deformation Field within Commercial Nanodiamonds Muhammad Salman Maqbool David Hoxley Nicholas W . Phillips , Hannah D . Coughlan Ross Harder. *Int. J. Nanotechnol.* **2017**, *14*, 251–264.
(14) Holler, M.; Guizar-Sicairos, M.; Tsai, E. H. R.; Dinapoli, R.; Müller, E.; Bunk, O.; Raabe, J.; Aeppli, G. High-Resolution Non-Destructive Three-Dimensional Imaging of Integrated Circuits. *Nature* **2017**, *543* (7645), 402–406. https://doi.org/10.1038/nature21698.
(15) Hÿtch, M.; Houdellier, F.; Hüe, F.; Snoeck, E. Nanoscale Holographic Interferometry for Strain Measurements in Electronic Devices. *Nature* **2008**, *453* (7198), 1086–1089. https://doi.org/10.1038/nature07049.
(16) Hÿtch, M. J.; Minor, A. M. Observing and Measuring Strain in Nanostructures and Devices with Transmission Electron Microscopy. *MRS Bull.* **2014**, *39* (02), 138–146. https://doi.org/10.1557/mrs.2014.4.
(17) Fluegel, B.; Mialitsin, A. V.; Beaton, D. A.; Reno, J. L.; Mascarenhas, A. Electronic Raman Scattering as an Ultra-Sensitive Probe of Strain Effects in Semiconductors. *Nat. Commun.* **2015**, *6* (May), 7136. https://doi.org/10.1038/ncomms8136.
(18) Huber, A. J.; Ziegler, A.; Köck, T.; Hillenbrand, R. Infrared Nanoscopy of Strained Semiconductors. *Nat. Nanotechnol.* **2009**, *4* (3), 153–157. https://doi.org/10.1038/nnano.2008.399.
(19) Yano, T.; Ichimura, T.; Kuwahara, S.; H'Dhili, F.; Uetsuki, K.; Okuno, Y.; Verma, P.; Kawata, S. Tip-Enhanced Nano-Raman Analytical Imaging of Locally Induced Strain Distribution in Carbon Nanotubes. *Nat. Commun.* **2013**, *4*, 1–7. https://doi.org/10.1038/ncomms3592.
(20) Rugar, D.; Budakian, R.; Mamin, H. J.; Chui, B. W. Single Spin Detection by Magnetic Resonance Force Microscopy. *Nature* **2004**, *430* (6997), 329–332. https://doi.org/10.1038/nature02658.

(21) Grinolds, M. S.; Warner, M.; De Greve, K.; Dovzhenko, Y.; Thiel, L.; Walsworth, R. L.; Hong, S.; Maletinsky, P.; Yacoby, A. Subnanometre Resolution in Three-Dimensional Magnetic Resonance Imaging of Individual Dark Spins. *Nat. Nanotechnol.* **2014**, *9* (4), 279–284. https://doi.org/10.1038/nnano.2014.30.

(22) Pioro-Ladrière, M.; Obata, T.; Tokura, Y.; Shin, Y.-S.; Kubo, T.; Yoshida, K.; Taniyama, T.; Tarucha, S. Electrically Driven Single-Electron Spin Resonance in a Slanting Zeeman Field. *Nat. Phys.* **2008**, *4* (10), 776–779. https://doi.org/10.1038/nphys1053.

(23) Neumann, J. T.; Garbowski, T.; Högele, W.; Korb, T.; Halder, S.; Leray, P.; Garreis, R.; le Maire, M.; Zeidler, D. High-Throughput Multi-Beam SEM: Quantitative Analysis of Imaging Capabilities at IMEC-N10 Logic Node; Sanchez, M. I., Ukraintsev, V. A., Eds.; 2017; p 101451S. https://doi.org/10.1117/12.2257980.

(24) Paine, B. M.; Hurvitz, N. N.; Speriosu, V. S. C. Strain in GaAs by Low-dose Ion Implantation. *J. Appl. Phys.* **1987**, *61* (1335). https://doi.org/10.1063/1.338112.

(25) Ziegler, J. F.; Biersack, J. P. The Stopping and Range of Ions in Matter. In *Treatise on Heavy-Ion Science*; Springer US: Boston, MA, 1985; pp 93–129. https://doi.org/10.1007/978-1-4615-8103-1_3.

(26) Wahl, U.; Vantomme, A.; De Wachter, J.; Moons, R.; Langouche, G.; Marques, J. G.; Correia, J. G. Direct Evidence for Tetrahedral Interstitial Er in Si. *Phys. Rev. Lett.* **1997**, *79* (11), 2069–2072. https://doi.org/10.1103/PhysRevLett.79.2069.